Available online at www.sciencedirect.com
SCIENCE DIRECT
International Journal of Mass Spectrometry 245 (2005) 1–13
International Journal of Mass Spectrometry
www.elsevier.com/locate/ijms

Review

Structure determination of gaseous metal and semi-metal cluster ions by ion mobility spectrometry

Patrick Weis *

Institut für Physikalische Chemie, Universität Karlsruhe, 76128 Karlsruhe, Germany

Received 27 April 2005; received in revised form 21 June 2005; accepted 23 June 2005
Available online 21 July 2005

Abstract

Gas phase ion mobility spectrometry in combination with quantum chemical calculations has proven to be extremely useful for the structure determination of cluster ions. After a short introduction into the methodology, investigations focused on clusters of different main group metals and semi-metals are reviewed. Based on the findings of different groups, it became apparent that in many cases small clusters (below 100 atoms) show a rich variation in shape as function of the number of atoms.

Keywords: Metal; Cluster; Ion; Mobility

Contents

* Tel.: +49 721 608 3306; fax: +49 721 608 7232.
E-mail address: patrick.weis@chemie.uni-karlsruhe.de.

1387-3806/$ – see front matter © 2005 Elsevier B.V. All rights reserved.
doi:10.1016/j.ijms.2005.06.005

1. Introduction

The investigation of the motion of ions in gases dates back to early works of Townsend [1], in the late 19th century. In the 1930s, it was Tyndall [2] who gave new impetus to the field with the first accurate mobility measurements of alkali ions in a drift cell filled with rare gases. The investigations of the following decades were mostly focused on small atomic or molecular ions in gases like nitrogen, oxygen and rare gases [3]. In the 1970s, ion mobility spectrometry was established as an analytical method for the detection of organic molecules [4,5]: as bath gas in the drift cell nitrogen or air was used under ambient conditions, a common method to ionize the organic sample was with the radiation of a radioactive source like ^{63}Ni. The drift time distribution of the (fragment-) ions through the gas gives a "finger print" spectrum of the substance investigated—in some respects analogous to a gas chromatogram. The devices are rather rugged, compact and mobile. Nowadays, they are in use, for example, in airports as a tool to detect traces of drugs and explosives [6–9].

Ion mobility spectrometry as a method to determine the structure of large molecular ions was established in the 1990s by Bowers and coworkers [10,11] and Jarrold and Constant [12]. The crucial improvement was the combination with mass spectrometers before and after the drift cell. With this setup it was possible to measure the drift time distribution of only one ionic species—fragmentation and/or reaction products were rejected in the mass spectrometers. Furthermore, the combination with modern ionization methods such as matrix assisted laser desorption/ionization (MALDI), electrospray ionization (ESI) and laser vaporization made gas phase measurements available for new substance classes, such as peptides, nucleotides, synthetic polymers and clusters. In the case of oligopeptides, Jarrold and coworkers [13–21] showed with drift time measurements that depending on the amino acid sequence, globular or helical structures are preferred. Bowers and coworkers investigated the gas phase conformation of the peptides [22–24], oligonucleotides [25–31] and synthetic polymers [32–35]. Clemmer and coworkers developed the ion mobility technique into a tool for high-throughput screening of peptide mixtures [36–40]. The application of ion mobility spectrometry as a tool to determine the structure of biomolecules has been the focus of several recent reviews [41–43]. The focus of this article will be on the use of ion mobility spectrometry as a tool to determine the structure of cluster ions.

2. Ion mobility spectrometry as a tool to obtain structural information

Gas phase ion mobility spectrometry is a straightforward, albeit not model-free way to gain structural information on an ionic species. In this method, the cluster ion is injected into a gas filled drift cell and guided by a weak electrical field. The collision cross-section of the ion is determined under thermal conditions by determining its drift time as function of bath gas pressure and electrical field strength. This collision cross-section can be directly compared with structure predictions based on quantum chemical calculations—this close connection between experiment and theory is an important advantage of the method. (A prerequisite is however, that the motion of the cluster ion in the bath gas is essentially diffusive, i.e., the electrical field must be weak enough to represent only a small perturbation.) The average drift time t of an ion in a bath gas is given by:

$$v_\mathrm{d} = \frac{L}{t} = KE = K\frac{U}{L} \quad \text{and therefore} \quad K = \frac{L^2}{Ut}$$

where v_d is the average drift velocity, L the length of the drift region, E the electrical field strength and U is the corresponding voltage. K represents the mobility of the cluster ion in the respective bath gas. The ion mobility is connected with the collision cross-section by [3]:

$$K = \frac{3q}{16N}\sqrt{\frac{2\pi}{\mu k_\mathrm{B} T}}\frac{1}{\Omega}$$

where N is the number density of the bath gas in the cell, μ the reduced mass of ion and bath gas molecule and Ω is the (experimental) collision cross-section. This is the connection to quantum chemical calculations. The theoretical collision cross-section depends on the structure of the cluster ion and the interaction potential between this ion and the bath gas molecules. Depending on the nature of the bath gas and the cluster ion considered, this interaction potential will comprise charge–dipole, charge-induced dipole, dipole–dipole as well as van der Waals interactions. Choosing helium as bath gas greatly simplifies the situation: it has no dipole moment, its polarisability is extraordinarily low—thus, the interaction between cluster ion in helium atom can be treated in a reasonable approximation as an elastic scattering of hard particles. The cross-section of a cluster ion drifting in helium should therefore reflect its geometric shape. A simple way to calculate the collision cross-section of a cluster ion with given molecular geometry is therefore the hard spheres model: each

atom of the cluster is replaced by a sphere with an element-specific radius. Within this model, the cross-section of the whole molecule can be determined by averaging over a sufficient number of orientations (projection approximation, PA). The projection approximation is however only correct for particles built of hard spheres if they are convex. For concave bodies, one has to consider multiple collisions (i.e., the scattered bath gas atom hits another part of the cluster ion). This has been taken into account in the so-called "exact hard spheres scattering model" (EHSS) [44] developed by the group of Jarrold. For small cluster ions, the difference between the two models is often small, simply because they usually have a rather compact, mostly convex shape and are too small for multiple collisions.

If the calculated cross-sections and the experimental values agree within the combined uncertainties of theory and experiment (typically ±2%) a structure can be considered as confirmed, otherwise it can be ruled out. This trial and error approach has proven to be an extremely useful tool for the structure determination of gaseous cluster ions.

3. Application of ion mobility spectrometry to cluster ions

3.1. Pure carbon clusters

In 1991, Helden et al. [11] revealed the structures of the cationic carbon clusters formed upon laser vaporization of a carbon rod. They found several families of coexisting isomers: up to C_{10}^+ they found linear chains, in the range between 7 and 40 carbon atoms they observed monocyclic rings, followed by polycyclic rings starting at 21 carbon atoms and finally cage-like fullerene structures starting at 30 atoms.

In 1993, Helden et al. [45,46] and Hunter et al. [47] injected carbon clusters (made by laser vaporization of graphite) into the drift cell with high energies (several 100 eV laboratory frame) showing that large polycyclic carbon clusters (50–70 atoms) can be efficiently annealed into fullerene structures thereby shedding light into the still mysterious process of fullerene formation. For clusters with 30–50 atoms, Hunter et al. [48] found that the polycyclic rings (that are predominantly formed in the laser vaporization source in this size range) anneal into both monocyclic rings and fullerenes. In the range between 10 and 36 atoms, they found that the monocyclic ring is the dominant isomer after annealing [49].

Bowers and coworkers [50] investigated the effect of charge state on the cluster topology—in anionic carbon clusters they found linear chains with up to 20 atoms, in strong contrast to previous findings on positively charged carbon clusters were linear chains where only found up to $n = 10$. They also investigated the effect of hydrogen on the carbon cluster growth by adding 10% hydrogen to the expansion gas in the laser vaporization source [51] and found that under these conditions the fullerene formation is efficiently quenched, while linear chains and monocyclic rings dominate for up to 20 carbon atoms. The structures to compare the experimental cross-sections with were calculated with the semi-empirical PM3 method. With respect to the relative amounts of linear chains and monocyclic rings, positively charged $C_nH_2^+$ and anionic C_n^- clusters quantitatively agree in the size range between 5 and 20 carbon atoms. In the studies mentioned so far, the carbon clusters were made by laser vaporization of graphite. In 1994, Hunter and Jarrold [52] investigated the C_{120}^+ ions formed by laser desorption of C_{60} and found two isomeric forms in the arrival time distribution, one could be attributed to a large closed cage fullerene structure, the other to a C_{60}-dimer (the structure of which could not be completely revealed at that time). In the years to come, Jarrold and coworkers revisted the issue of fullerene coalescence with higher experimental resolution and improved theoretical methodology [53,54]. They concluded that the dimeric form is a [2 + 2]cycloadduct. In the plasma formed upon the vaporization of C_{60} they found for the even numbered cluster sizes above C_{120}, additional isomers, so called "ball-and-chain dimers" representing two fullerene cages linked by a chain with up to eight carbon atoms [55].

3.2. Doped carbon clusters

Bowers and coworkers [56] investigated the structures of small iron carbon cluster anions (Fe_xC_y, $x = 1$–3, $y = 2$–8) and found for $x = 1$ both linear chains and planar clusters. For $x = 2$, they found ring structures with a Fe_2 unit incorporated, and for the clusters with three iron atoms they observed three-dimensional structures. Fye and Jarrold [57] investigated the structures of C_nSi^+ ($n = 3$–69) made by laser vaporization of a mixture of graphite and silicon. They found essentially the same structures as for the respective pure carbon clusters, i.e., with increasing cluster size chains, rings and cages. In carbon clusters doped with a single palladium atom (by laser vaporization of a Pd/graphite mixture) on the other hand, no fullerene-like cages were found in the range between 10 and 60 carbon atoms [58]. For carbon clusters containing one or two lanthanum atoms, LaC_n^+ and $La_2C_n^+$ (by laser vaporization of LaC_2/graphite mix) Shelimov et al. [59–61] showed a strong preference for the endohedral position for the first lanthanum atom, while the second lanthanum atom can be incorporated both inside and outside the cage. Based on the drift time distributions they concluded that for the carbon clusters with two lanthanum atoms new isomeric forms that are not present in the pure carbon clusters can be found.

Carbon clusters doped with one niobium atom NbC_n^+ ($n = 15$–50) show as function of size essentially the same families of isomers (monocyclic rings – polycyclic rings – fullerenes) as the pure carbon clusters, but at different abundances [62].

3.3. Metal and semiconductor clusters

Ion mobility spectrometry as a tool to elucidate the structure of metal cluster ions has been extensively applied by Jarrold and coworkers on metal clusters of rows 13 and 14.

3.3.1. Aluminum

For aluminum [63,64], they investigated both singly and doubly charged cluster cations in the size range between 5–73 atoms (Al_n^+) and 20–142 atoms (Al_n^{2+}). They found that the cross-sections of these clusters are almost independent of the charge state, albeit there are strong modulations as function of the size of the cluster. The observed maxima in ion mobility (corresponding to compact structures) were found to correspond to regions of electronic shell closings of the jellium model (20, 40, 58, 92, . . . valence electrons).

3.3.2. Indium

Lermé et al. [65] investigated the mobilities of positively and negatively charged indium clusters $In_n^{+/-}$ for sizes between 2 and 30 atoms. In this size range, indium clusters are believed to be liquid at room temperature [66] and therefore, their geometric shape is expected to be close to spherical. In the ion mobility measurements, they found that the cross-sections of the anions are systematically larger than the respective cationic values. This can be explained in terms of a more extended electron cloud for the anionic clusters, which in turn means that the mobility of a cluster ion is not only a function of the positions of the atoms constituting the cluster, but also of its electron density distribution. For atomic ions of transition metals such an influence of the electronic state on the ion mobility has been shown by Helden et al. [67].

3.3.3. Silicon

In a series of experiments, Jarrold and coworkers revealed the main structural features of positively and negatively charged silicon clusters with up to 60 atoms [68–70]. Compared to carbon clusters with their preference for chains, rings and finally fullerenes with increasing cluster size, completely different structural motifs were found, i.e., early occurrence of three-dimensional structures. In the size range between 12 and 18 atoms, they observed prolate structures based on stacked Si_9 tricapped trigonal prisms followed by compact, quasi-spherical structures for the larger clusters. By comparing the experimental cross-sections with predictions from theory (based on an unbiased global minimum search by a genetic algorithm and geometry optimizations at the DFT level) they could in many cases assign the exact cluster geometries. By repeating the measurements with an improved setup with significantly higher resolution [70], they were able to identify a large number of different isomers in the transition region between prolate and quasi-spherical structures (around 20–30 atoms).

3.3.4. Germanium

In a similar study on germanium clusters, Jarrold and coworkers could show that in the range below approximately 20 atoms, germanium clusters follow the same principles as the silicon clusters (prolate structures that are based on tricapped trigonal prisms) but the geometries differ in some details [71]. The transition to quasi-spherical structures occurs however at significantly larger cluster sizes, around $n = 65$ [72].

3.3.5. Tin

The morphology of positively charged tin clusters follows the same trend as found for silicon and germanium: the smaller clusters are prolate (up to $n = 35$), the larger ones arrange in near-spherical geometries [73]. It is interesting to note that small tin clusters (in the range between 10 and 30 atoms) retain their prolate shape (and therefore a comparatively large cross-section) and do not convert into spherical geometries, even when heated up to 555 K, 50 K *above* the melting point of bulk tin [74]. Such a non-spherical shape implies that the cluster is still solid at that temperature (although there is no strict thermodynamic definition of the melting point for small clusters, one can assume that a molten cluster has in the time average a compact, almost spherical structure with a smaller collision cross-section).

3.3.6. Lead

The cross-sections of positively charged lead clusters (size range up to $n = 32$) are significantly smaller than respective values of their lighter element cluster congeners [75]. This implies that Pb_n^+ ions favor compact, near-spherical geometries, already at small cluster sizes unlike silicon, germanium and tin, which first grow in prolate geometries. In other words, at least in terms of geometry small tin clusters behave more like germanium and silicon than lead and one might speculate that for small group 14 clusters the transition between covalent and metallic behavior is between tin and lead.

3.4. Coinage metal clusters, silver

In our measurements, we have focused on clusters of coinage metals, i.e., copper, silver and gold. The coinage metals are “simple” metals in the sense that the d-shell is completely filled and their chemistry is determined by the single s valence electron—like in the alkali metals. This picture is adequate at least for silver and significantly simplifies its theoretical treatment. Accordingly, there are numerous quantum chemical calculations on small silver clusters [76–81] as well as experimental investigations like, for example, photo-dissociation spectroscopy [82–84], femto-second spectroscopy [85,86], fluorescence measurements in rare gas matrix [87] to give just a few recent examples. On the other hand, the equilibrium structures of even the smallest clusters are still subject to controversy. In this respect, the determination of the collision cross-section is a suitable tool to gain more structural information.

Details of our experimental setup are described in detail in an earlier publication [88]. In brief, the apparatus comprises a combination of a time-of-flight mass spectrometer, an ion mobility drift cell and a quadrupole mass filter. The cluster ions are produced by laser vaporization (vaporization laser: Continuum ND 61, second harmonic, 30 Hz repetition rate) in a variant of a Smalley-type setup [89], with helium (pulsed, backing pressure 5–10 bar) as cooling gas. The clusters expand with the cooling gas through a nozzle into the high vacuum of the source chamber. A particular cluster size is selected in the time-of-flight mass spectrometer, injected into the drift cell (110 mm long, filled with 5–10 mbar helium, 0.5 mm diameter entrance and exit orifices). The ion packet drifts through the cell under the influence of a weak electric field (drift voltage 50–300 V) and its arrival time is determined as function of the applied drift field. A quadrupole mass filter (Extrel) behind the cell rejects possible fragmentation products. The ions are detected by means of a channeltron electron multiplier and counted by an EG&G MCS board (2 μs dwell time). From the arrival time distributions as functions of the helium pressure in the drift cell and the applied electric fields the collision cross-sections can be easily determined (cf. [88]).

Fig. 1 shows the collision cross-sections of the silver cluster cations [90]. They increase monotonically, roughly proportional to the number of atoms to the power of 2/3, as expected for quasi-spherical clusters (see fit function in Fig. 1). However, there are significant deviations for small cluster sizes, as can be clearly seen when looking at the relative cross-sections, i.e., by dividing the measured collision cross-sections by the fit function (see Fig. 2). For structural assignment, the experimental data are compared with predictions based on quantum chemical calculations. We used both MP2 and density functional theory (DFT, BP-86 parameterization [91]) as implemented in the TURBOMOLE package [92] to find reasonable candidate structures by geometry optimization, i.e., search for energy minima. The inner shell

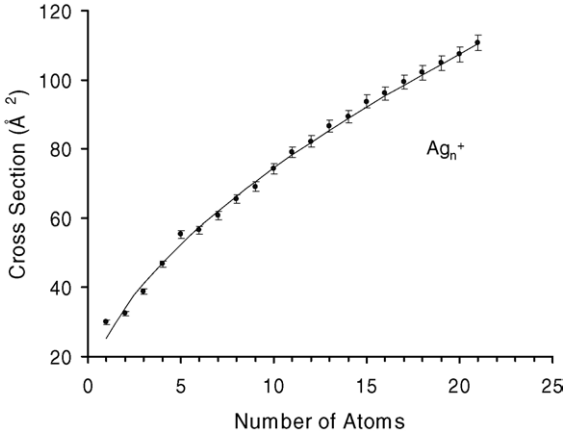

Fig. 1. Collision cross-sections of Ag_n^+ clusters. The line is a fit for quasi-spherical clusters with the fit function $\Omega(n) = 4/3\pi(N^{1/3}r_{Ag} + r_{He})^2$; N is the number of atoms in the cluster ion and the parameters r_{Ag} and r_{He} were determined to 1.52 and 0.94 Å, respectively.

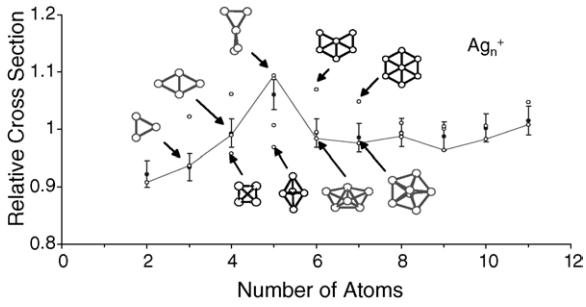

Fig. 2. Relative collision cross-sections of the silver cluster cations, comparison of the experimental data (●) with quantum chemically computed structures (◯). The line connects the collision cross-sections of the global minima calculated at MP2 level.

electrons of each silver atom are treated by means of the relativistic effective core potential (ECP) of the Stuttgart group [93], only the 19 outermost electrons, i.e., the 5s-shell and the 4s-, 4p-, 4d-shells are treated explicitly. The valence basis set for Ag is based on TURBOMOLE's standard SVP basis augmented by additional polarization and diffuse functions resulting in a (6s5p3d1f) [8s7p5d1f] basis [90].

For the trimer Ag_3^+ only one minimum structure can be found with both methods, an isosceles triangle. For the tetramer Ag_4^+, three local minima exist—a diamond, which represents the global energy minimum, as well as a Y-shaped and quasi-tetrahedral structure. Both are however more than 0.2 eV higher in energy. The lowest energy structure of the pentamer consists of two Ag_3 triangles with a common central atom—the trigonal bipyramid is a local minimum at both MP2 and DFT level, but more than 0.2 eV less favorable. At the hexamer the predictions of both methods diverge: MP2 favors a three-dimensional structure that can be looked upon as two tetrahedrons sharing a common edge, DFT predicts a planar structure. The same holds true for the heptamer. Starting at Ag_8^+ both methods exclusively find three-dimensional structures. Comparison of calculated and measured cross-sections confirms the MP2 results—for the pentamer the trigonal bipyramid can be definitely ruled out, for the tetramer only the cross-section of the diamond is in agreement with the experimental value. Hexamer and heptamer are three-dimensional, as predicted by the MP2 calculations (see Fig. 2). The structures are mostly in line with predictions of Bonačić-Koutecký et al. [94]—except for Ag_5^+ for which a trigonal bipyramid is found as global minimum.

3.5. Copper

The collision cross-sections of the positively charged copper clusters are generally somewhat smaller than the values of the respective silver clusters. Their trend, as function of cluster size, does however strongly resemble the experimental results for the corresponding silver clusters. Like for silver, the candidate structures for comparison with the experimental data were obtained by full geometry optimizations at both DFT and MP2 level with TURBOMOLE's standard

SVPP basis. Both methods yielded very similar results, i.e., same structures with comparable binding energies. Up to the octamer, the same global minima were found with both methods, they are topologically identical with the respective silver structures (except for the pentamer, see below): the trimer is an isosceles triangle, the tetramer has a diamond-like structure. For the hexamer, the 3D structure is more than 0.3 eV lower in energy than the planar geometry. The lowest Cu_7^+ structure is the pentagonal bipyramid, followed by another 3D structure with C_{3v} symmetry that can be looked upon as composed of four face-sharing tetrahedrons. The planar D_{6h} structure is, unlike in the case of the silver heptamer, not a local minimum.

For Cu_5^+, the situation is somewhat complicated—at DFT-level, we found five different structures within 0.05 eV: like in Ag_5^+, there is the motif of the two triangles sharing a common central atom, in the planar D_{2h} geometry this represents a flat saddle point, while the twisted D_{2d} arrangement is a local minimum. Another variant of this motif, two triangles in a planar W-geometry is the global minimum at DFT level. However, we find two three-dimensional structures within the 0.05 eV energy interval as well—the trigonal bipyramid and a topological very similar structure with C_{2v} symmetry. At MP2 level, the W-structure does not represent a local minimum, the respective calculation converges into the D_{2h} geometry. As global minimum MP2 predicts the D_{2d} structure, the trigonal bipyramid is roughly 0.1 eV higher in energy. Comparison of the cross-sections of these structures with experiment clearly favors the W-structure, i.e., the prediction at DFT-level (Fig. 3). Furthermore, the comparison of the experimental and calculated cross-sections clearly shows that cationic copper clusters with more than six atoms are three-dimensional. For the heptamer, the three-dimensional C_{3v} structure agrees best with the experimental cross-section, the energetically favored pentagonal bipyramid is slightly below the experimental value. In this case, a definite assignment cannot be given, a planar geometry can however be clearly ruled out. The structures that we find are in most cases in agreement with predictions of Jug et al. [95], except for the pentamer, where they predict the trigonal bipyramid, a structure that can be clearly ruled out based on our experiments.

To summarize the results for copper and silver cations, the transition to three-dimensional structures is at a cluster size of six atoms, the triangle is a very important structural motif: all structures, planar as well as three-dimensional, are composed of (almost isosceles) triangles sharing edges.

3.6. Gold cations

In its experimental collision cross-sections cationic gold clusters [96] show significant deviations compared to their lighter element congeners, as can be clearly seen in a direct comparison of the *relative* collision cross-sections of Cu_n^+, Ag_n^+ and Au_n^+ (Fig. 4). It is obvious that the 6-, 7-, 9- and 11-atom gold clusters are much bigger than the respective silver and copper clusters. As mentioned before, in order to actually assign structures, support from quantum chemical calculations is needed. The same methods as for copper and silver, DFT-BP86 and MP2 were used in the search for reasonable candidate structures. Analogous to silver, the 5s, 5p, 5d and 6s electrons of each gold atom are treated explicitly, the remaining electrons are replaced by an effective core potential [93] with a valence basis set based on TURBOMOLE's SVP set, augmented by polarization and diffuse functions resulting in a (9s7p5d1f)/[7s5p3d1f] valence basis set [96]. In the theoretical treatment of gold it is crucial that this effective core potential takes into account (scalar) relativistic effects, i.e., the lowering of the 6s orbitals compared to the 5d orbitals [97]. This leads to a much more efficient s–d-hybridization, compared to the situation in silver—and therefore to different minimum structures in many cases. For the gold trimer and tetramer, the same geometries as for the respective copper and silver clusters are found, the isosceles triangle and

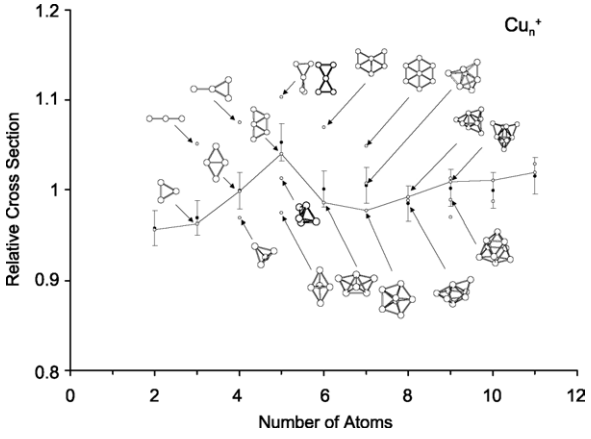

Fig. 3. Relative collision cross-sections of the copper cluster cations, comparison of the experimental data (●) with quantum chemically computed structures (○). The line connects the collision cross-sections of the global minima calculated at DFT level.

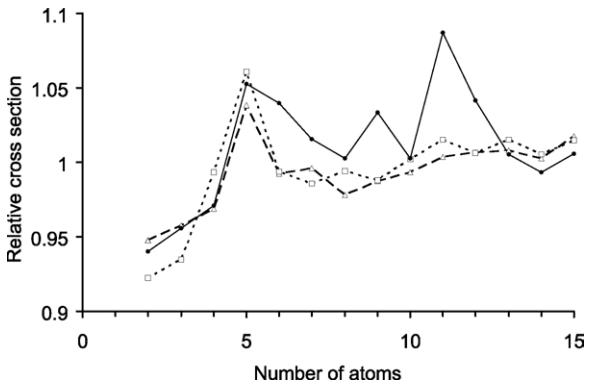

Fig. 4. Relative collision cross-sections of the different coinage metal cluster cations (division of the measured cross-sections by a quasi-spherical fit (cf. Fig. 1). Fit parameters: r_{Cu} = 1.37 Å, r_{Ag} = 1.52 Å, r_{Au} = 1.56 Å, r_{He} = 0.94 Å. Au_n^+: full line and circles (●), Ag_n^+: dotted line and squares (□) and Cu_n^+: dashed line and triangles (△).

the diamond. The gold pentamer has the same X-structure as Ag_5^+, the trigonal bipyramid is according to the calculations roughly 0.5 eV higher in energy. For the hexamer, both DFT and MP2 predict slightly different, but *planar* geometries. The DFT global minimum structure consists of an isosceles triangle with three atoms one each edge, the MP2 favors a structure consisting of two diamonds sharing a common edge. The lowest 3D structure is according to both methods significantly higher in energy (MP2: +0.2 eV, DFT: +0.5 eV). The same holds true for Au_7^+: both methods predict a planar global minimum, the D_{6h} ring with six-fold coordinated central atom. The pentagonal bipyramid, the "best" 3D structure, is more than 0.2 eV higher in energy. Up to this point the quantum chemical predictions are unequivocal—small cationic gold clusters, including hexamer and heptamer, should be planar. The cross-sections calculated for these structures are in almost perfect agreement with the experimental values (Fig. 5). To summarize, the predictions of the MP2 and DFT calculations can be confirmed, cationic gold clusters with up to seven atoms are planar. With the octamer, the situation becomes somewhat complicated—according to DFT this cluster should be planar as well, while MP2 favors the same 3D structure as in Cu_8^+ and Ag_8^+. When comparing these structures with experiment, one finds that the cross-section of the planar structure is significantly too high, while the MP2-optimum has a slightly too small value. The best fit is obtained for a (three-dimensional) local minimum, which is second best in energy (+0.25 eV) with both methods. In other words,

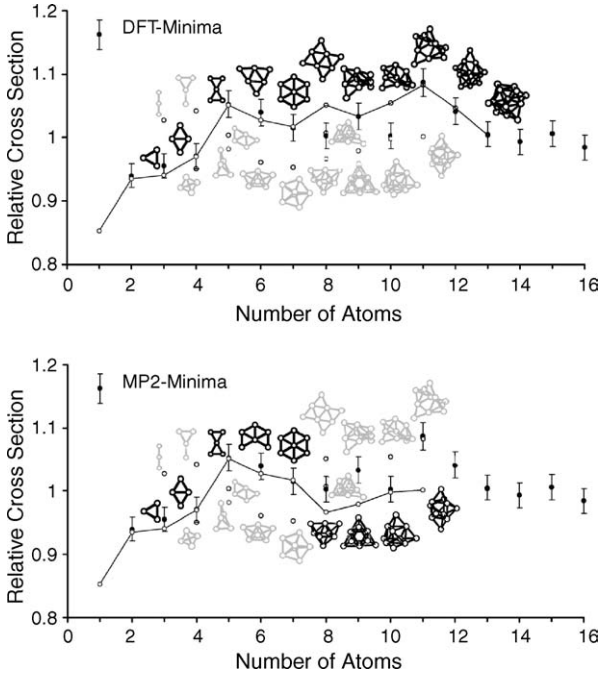

Fig. 5. Relative collision cross-sections of the gold cluster cations, comparison of experimental data (●) with quantum chemically computed structures (○), top: DFT and bottom: MP2 method. The full lines connect the collision cross-sections of the respective global minima (black structures). Other relevant structures are shown in grey.

the octamer is 3D—the planar structure can be ruled out. For Au_9^+ and larger gold clusters, both methods, DFT and MP2, predict only three-dimensional structures. Note that the unusually large cross-section of Au_{11}^+ does not result from a planar geometry—the energetically favored DFT structure is based on a trigonal prism, whose two trigonal faces and three edges are capped by another atom (D_{3h} symmetry)—pretty much like three spokes of a wheel. The structure is very open in the sense that each of the 11 atoms is located on the surface of the cluster—there is not a single atom that can be considered "inside". The cross-section of this structure is in almost perfect agreement with experiment.

3.7. Gold cluster cations: temperature-dependent measurements and dynamics

The results presented on the coinage metals so far were all obtained at room temperature. The arrival time distribution corresponds for all cluster sizes to the diffusion equation, i.e., the distribution has exactly the width that is expected for a single isomeric species. This however does not necessarily mean that only one isomer is present—two or more quickly converting structures will lead to a narrow, unstructured arrival time distribution, as long as the conversion rate is much faster than the average drift time. At sufficiently low temperatures such a conversion should freeze out giving rise to a bimodal arrival time distribution. Up to Au_{10}^+ we measured the ion mobilities at 77 K by flowing liquid nitrogen through the double walled drift cell [98].

Except for the nonamer all cluster sizes show only one maximum in their arrival time distribution (Fig. 6). For $n = 4$ and above, there is a small asymmetry in the arrival time distribution towards longer drift times, which can be most likely related to small amounts (<10%) of isomers with larger cross-sections formed upon injection into the drift cell. At very low injection energy this asymmetry disappears. For Au_9^+ however, the arrival time distribution is definitely bimodal (time difference of the peaks around 5%), indicative of the presence of two different isomers, roughly in a 1:2 ratio. The shape of the distribution is very robust—against variations of the source conditions (laser power, delays between gas pulse and laser, gas pressure) as well as of the injection energy (i.e., the kinetic energy with which the ions enter the drift cell): when increasing this injection energy to up to 300 eV (laboratory frame) we observe significant fragmentation into Au_8^+ and Au_7^+. The remaining Au_9^+ ions still show two peaks in their arrival time distributions. We injected Au_{10}^+ with 300 eV into the cell, causing it to fragment into Au_9^+, which had a bimodal distribution as well. To summarize, there are strong indications that the observed bimodal arrival time distribution of Au_9^+ reflects the thermodynamic stabilities of the constituting isomers and is not just a result of the (ill defined) aggregation kinetics in the cluster source. In order to shed more light into this issue, we measured the arrival time distributions of Au_9^+ in the range between 77 and 300 K as well. We find that in the region between 120 and 140 K

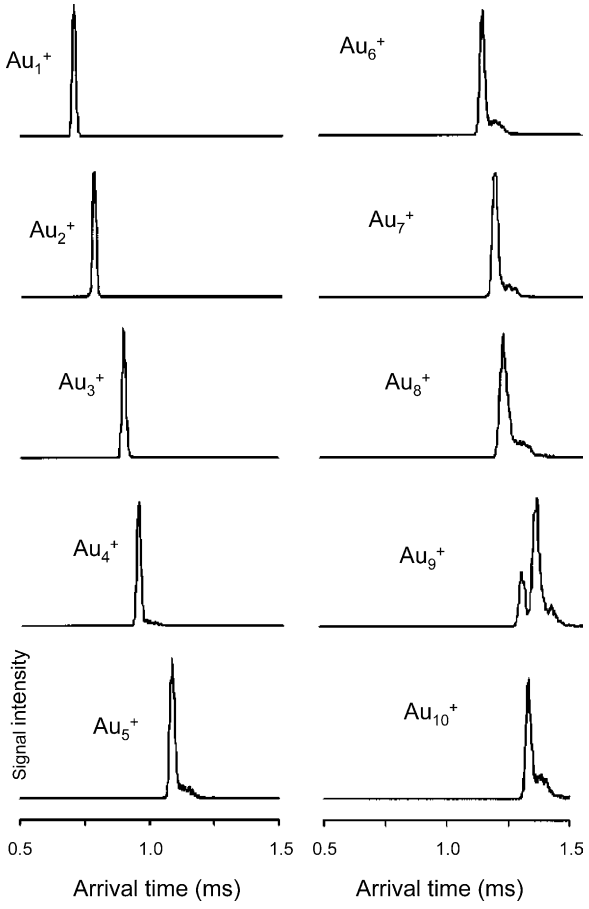

Fig. 6. Typical arrival times of Au_n^+ ($1 \le n \le 10$) at 77 K, a He pressure of 4.8 mbar and 200 V drift voltage. The distribution of Au_9^+ is bimodal, indicative of the presence of two isomeric species.

the bimodal distribution disappears and a broad, Gaussian like distribution prevails. With further increasing temperature the width of the distribution significantly decreases. Fig. 7 shows four typical arrival time distributions as well as simulations based on the diffusion equation for two different species coupled by a first-order conversion reaction. The only variable in the fit is the conversion time: at 77 K it is significant (more than 50-fold) *longer* than the drift time of roughly 1 ms, at 160 K the conversion is at least a factor of 10 *faster* than the drift time. At 140 K both time scales are comparable. This allows us to estimate the activation barrier to 0.1–0.2 eV. The remaining question is: what are the structures of the two isomers? MP2 and DFT predict slightly different (three-dimensional) structures as global minimum, the cross-sections of these structures differ by 5%. Furthermore, the conversion between the two structures requires only a small change in geometry, essentially the rearrangement of a single atom (Fig. 8). This interpretation remains somewhat speculative, i.e., we cannot rule out that other structures are involved as well. However, there are no doubts that Au_9^+ shows quick isomerization reactions far below room temperature.

3.8. Gold anions

The experimental cross-sections [99] of the negatively charged gold clusters show significant differences compared with the cationic gold clusters: the values of the anions are generally larger (up to $n = 15$, the largest anion measured), for the smaller clusters up to $n = 12$ by as much as 20% (see Fig. 9). For Au_{12}^-, a bimodal arrival time distribution is observed (at room temperature), i.e., two different isomers. For the large difference in cross-section between the two charge states, two possible explanations have to be taken into account: larger atomic radii of the anionic clusters or different structures. Larger atomic radii can be rationalized in terms of a more extended electron cloud, as has been observed in ion mobility measurements of indium clusters [65]. This effect should however quickly decrease with increasing cluster size since the influence of the additional electron is stronger for a small number of valence electrons. We observe such a convergence towards the cationic values between $n = 5$ and 6—but then the cross-sections of the anions (relative to the respective cations) increase again. This can only be explained in terms of structural differences between anionic and cationic gold clusters.

In the search for reasonable candidate structures we employed the same DFT-methodology (BP-86 functional, effective core potential, basis set) as for the investigation of the cationic gold clusters. The results are somewhat surprising—among the numerous local minima found for the different cluster sizes up to Au_{13}^-, planar structures were always energetically favored. For the trimer, a linear chain is the only minimum, the triangular structure of the cationic gold trimer is more than 1 eV higher in energy. For the tetramer, there are however three different isomers within 0.15 eV: favored by DFT is a zig–zag chain, followed by a Y-structure, which is 0.02 eV higher in energy. The diamond structure, the motif of the cationic coinage metal tetramers, represents a local minimum as well, it is however 0.14 eV above the chain. Based on the collision cross-section the chain and diamond can be ruled out, while the Y-structure is in agreement with experiment (see Fig. 10). For the pentamer, a W-structure is favored, for the hexamer an isosceles triangle, heptamer and octamer contain a central Au_4-square, all the larger clusters contain in the energetically favored structure a central Au_7-ring (see Fig. 10). All these global minima agree in their cross-sections with the experimental data, except for Au_{10}^- and Au_{13}^-. The Au_{10}^- structure favored by DFT, a triangle with four atoms per edge (10-1 in Fig. 10), has a somewhat too large cross-section. The "second best" minimum structure, planar as well and only 0.15 eV higher in energy is in perfect agreement with the experimental value. From the decrease in experimental cross-section between $n = 12$ and 13, it is clear that anionic gold clusters with 13 and more atoms are three-dimensional (albeit the DFT calculations favor for Au_{13}^- a planar structure). For Au_{12}^-, where two isomers are found in the cross-section measurement, one of these isomers corresponds to a planar,

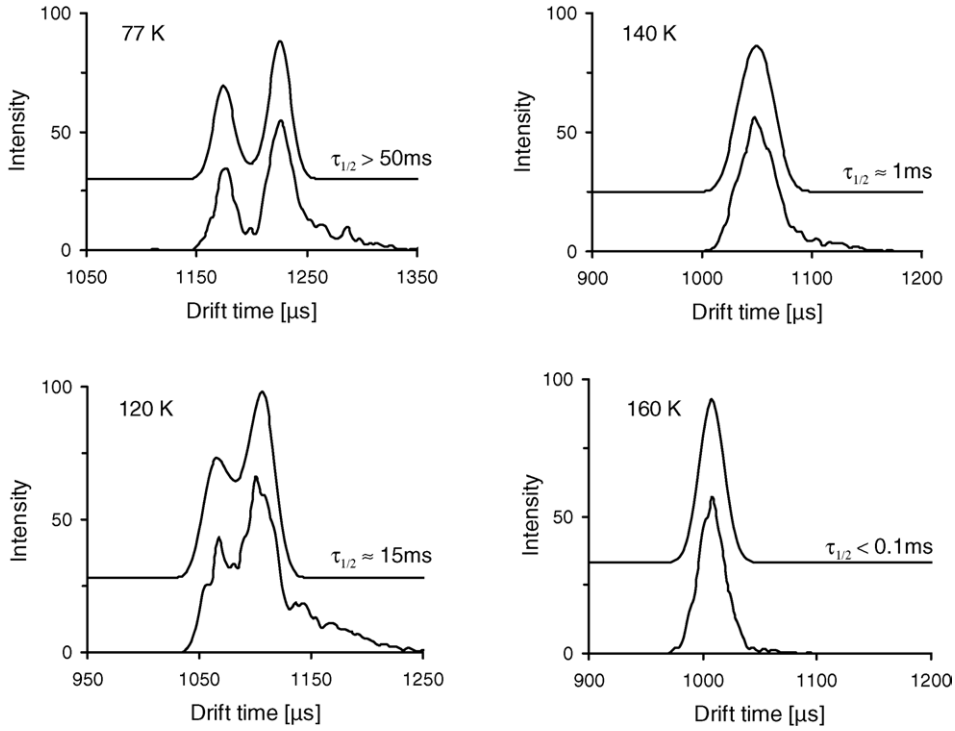

Fig. 7. Typical arrival times of Au_9^+ at four different temperatures. Lower lines: experimental arrival time distributions. Upper lines: simulated arrival time distributions based on two converting isomers (see also ref. [98]).

the other to a three-dimensional structure. To summarize, small gold clusters prefer planar geometries—for the cations (up to $n = 7$), as well as for the anions (up to $n = 12$). This is a result of the lowering of the 6s orbital (compared to the 5d-shell) due to relativistic effects. This enables a more efficient s–d-hybridization, leading to the formation of comparatively few, but more directed bonds and thus to the favorization of planar structures. It takes a comparatively large number of atoms for the typical metallic bonding behavior (with a large number of weaker bonds) to take over.

3.9. Mixed gold, silver and copper clusters

As mentioned before, pure gold and silver clusters differ significantly in their geometry—silver favors three-dimensional, gold planar structures. Mixed clusters of these metals have been investigated to a lesser extent—the dimers have been probed by fluorescence spectroscopy [100], up to the tetramers there is an investigation with photo-electron spectroscopy by Negishi et al. [101]. In a theoretical study Bonačić-Koutecký et al. [102] predicted the structures of the neutral and ionic bimetallic Ag–Au clusters up to the pentamer. In order to determine the structures experimentally, we made the different mixed cluster ions by laser vaporization using targets of the respective coinage metal alloys [103].

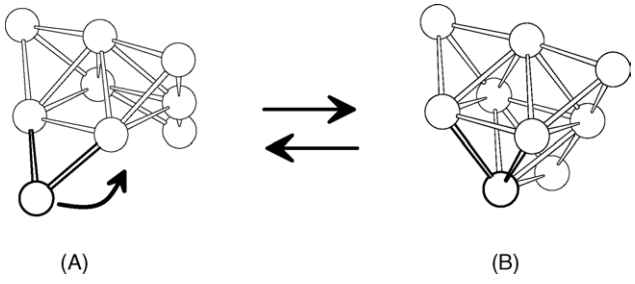

Fig. 8. Probable isomerization reaction of Au_9^+. The structures A and B represent the global energy minima found at DFT and MP2 level, respectively.

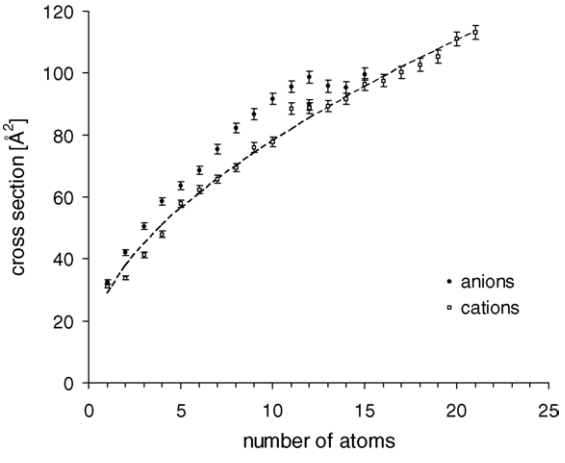

Fig. 9. Experimental collision cross-sections of the positively and negatively charged gold clusters. The line is a fit to the collision cross-sections of the cations.

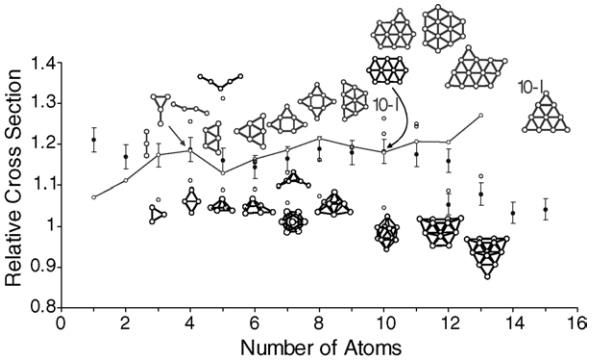

Fig. 10. Relative collision cross-sections of the gold cluster anions, comparison of experimental data (●) with quantum chemically (DFT) computed structures (◯). The line connects the collision cross-sections of the respective global minima (except Au_4^- and Au_{10}^-) shown in the upper part of the figure. The structures shown in the lower part of the figure represent energetically less favorable (three-dimensional) local minima, which mostly have much lower cross-section than found in the experiment.

3.9.1. Dimers

The measured cross-section of the dimer $AgAu^+$ does not interpolate the values of Au_2^+ and Ag_2^+, but is significantly larger. The same holds true for $CuAu^+$, but not for $CuAg^+$ (see Fig. 11). The unusually large cross-section of $AgAu^+$ cannot be explained by a larger bond length: according to a DFT calculation the bond distance of $AgAu^+$ is 2.67 Å, exactly in the middle between Ag_2^+ (2.72 Å) and Au_2^+ (2.62 Å). The accuracy of the calculation with respect to bond distances is usually better than 0.1 Å, in order to explain the large cross-section of $AgAu^+$ a bond length of more than 3 Å would be necessary, definitely beyond all reasonable error margins of the calculation. The reason for the large cross-sections lies in the charge distribution: the Ag–Au and Cu–Au bonds are polar, the silver (copper) atom carries a significant part of the positive charge. By including an asymmetric charge distribution in the cross-section calculation (i.e., the attractive interaction between the localized partial charges of the cluster ion and the He bath gas atoms), the experimental cross-section of $AgAu^+$ can be almost perfectly reproduced (see Fig. 12). Details of the methodology to include an asymmetric charge distribution in the cross-section calculation are given in [103]. In brief, the cluster–helium interaction is modeled by a Lennard–Jones potential plus charge-induced dipole interaction. The Lennard–Jones parameters for Ag–He

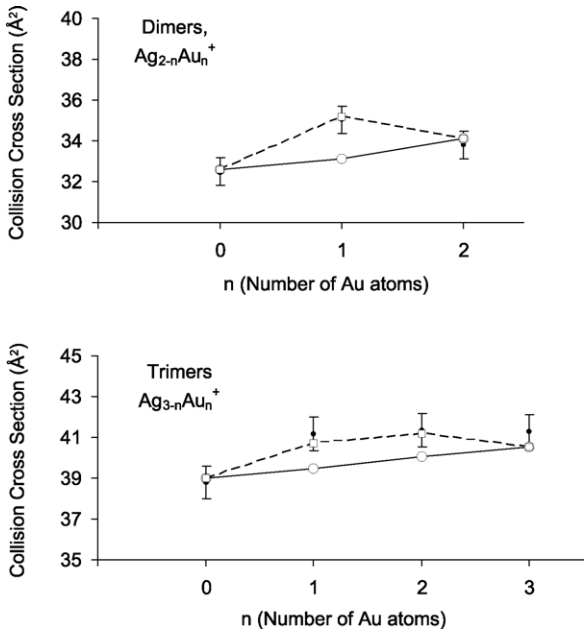

Fig. 12. Collision cross-sections of the silver–gold dimer and trimer cations. Full circles (●) and error bars correspond to the experimental data, open circles (◯) to the calculated cross-sections based on uniform charge distributions and the squares (□) correspond to calculated cross-sections with the positive charge largely located on the silver atoms (see [103]).

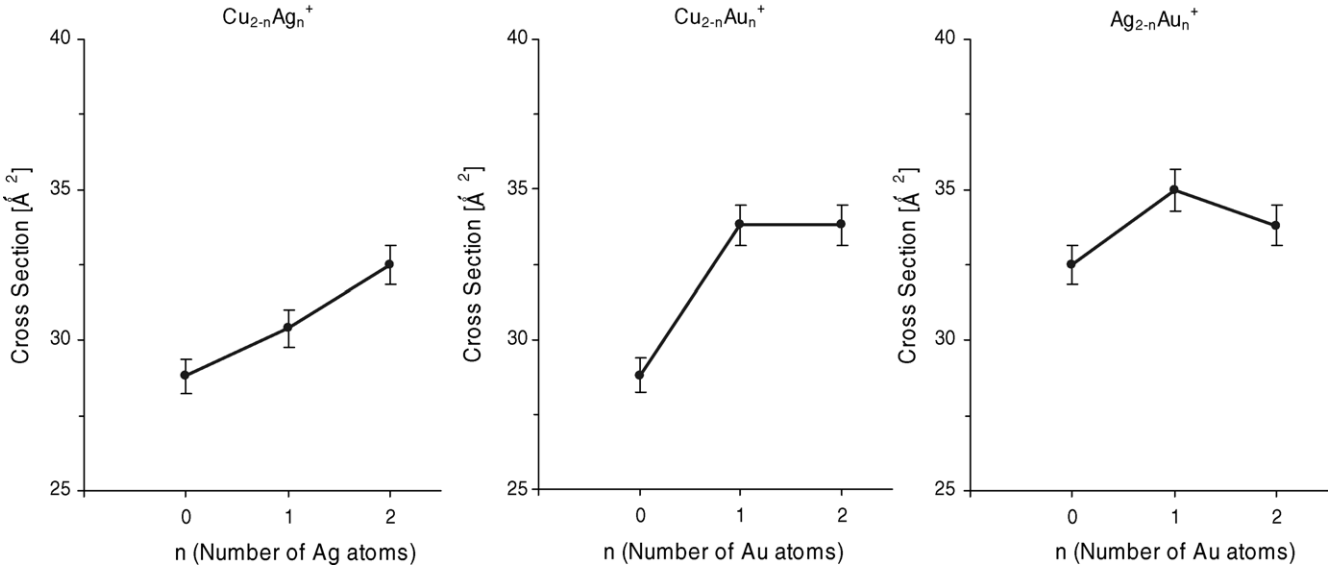

Fig. 11. Collision cross-sections of the mixed coinage metal dimers.

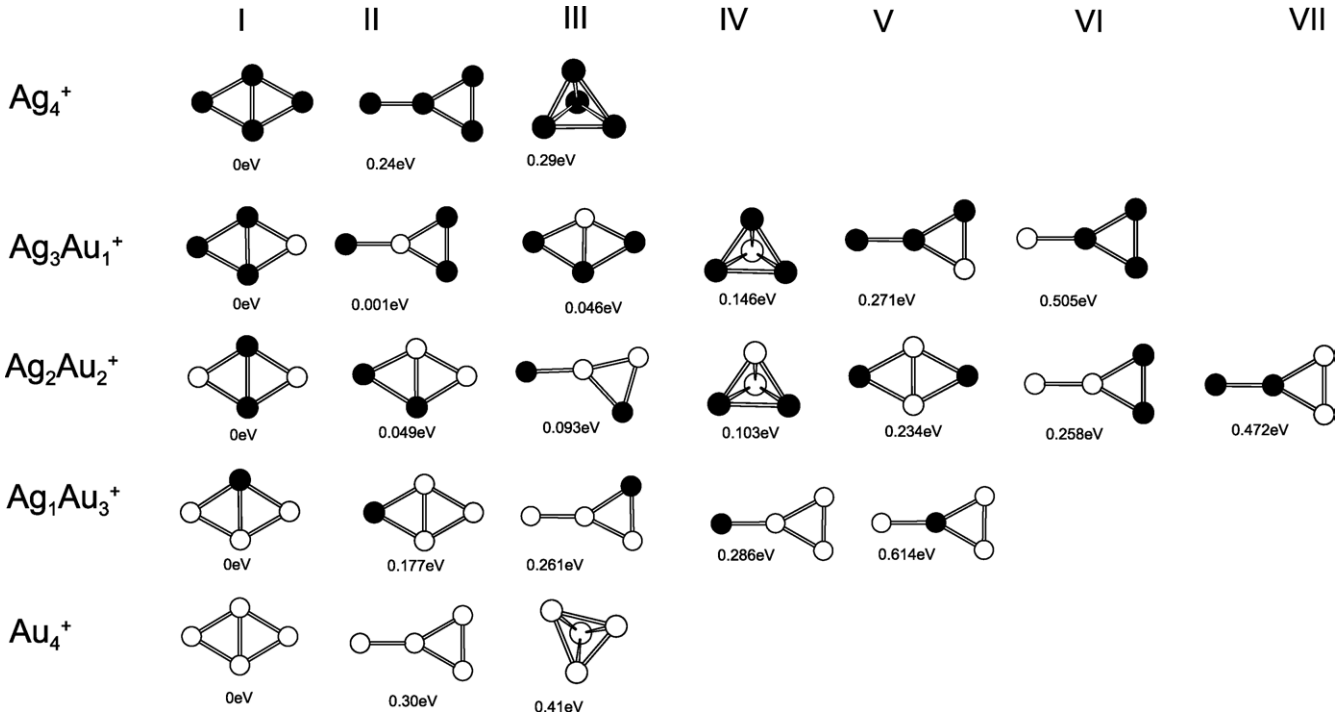

Fig. 13. Structures and relative energies for the pure and mixed tetrameric cations, optimized at DFT level. The different local minima are sorted in the order of increasing energy—the first column (I) corresponds to the global minima. Note that for Ag_3Au^+ isomers I and II are essentially isoenergetic.

and Au–He are adjusted to match the experimental cross-sections of the pure clusters (dimer to pentamer, least squares-fit).

3.9.2. Trimers

The mixed Au–Ag trimers Ag_2Au^+ and Au_2Ag^+ show also an increased collision cross-section compared to the pure Ag_3^+ and Au_3^+ clusters which cannot be rationalized in terms of structural differences (all trimers are triangles with similar bond lengths). The reason is again the asymmetric charge distribution (see Fig. 12).

3.9.3. Tetramers

While there are no relevant alternate isomeric forms for the mixed trimers and dimers, the situation is completely different for the tetramers: besides the different topologies diamond, Y-structure and tetrahedron that represent the local minima found in the DFT calculations of the pure Ag_4^+ and Au_4^+ clusters, in the mixed clusters different substitution isomers have also to be taken into account (Fig. 13). In Ag_3Au^+, the diamond and Y-structure are almost degenerate (within 0.001 eV), in all other tetrameric clusters the diamond is clearly favored. The comparison of the calculated cross-sections with the experimental values shows that Ag_3Au^+ has a Y-structure while the other clusters are diamond-shaped. Note also that at this cluster size and above the charge distribution is essentially irrelevant for the collision cross-section (see Fig. 14, full and dotted lines).

3.9.4. Pentamers

Among the pentamers only the arrival time distribution of $Ag_3Au_2^+$ is bimodal [103], all other clusters have only one isomer. This is in excellent agreement with predictions based

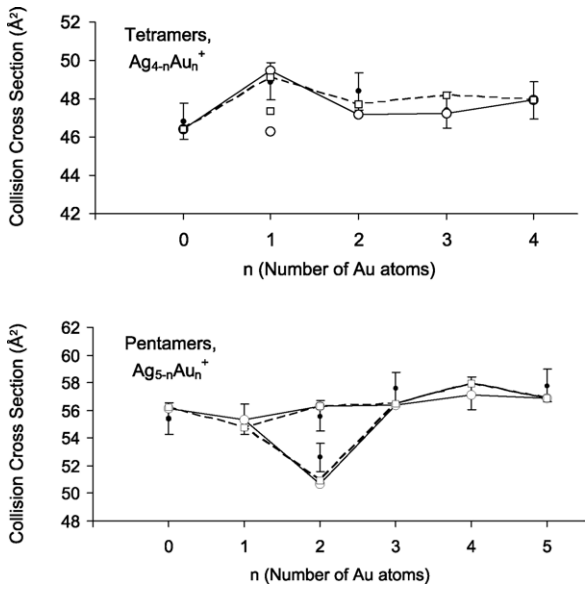

Fig. 14. Collision cross-sections of the silver–gold tetramer and pentamer cations. Full circles (●) and error bars correspond to the experimental data, open circles (◯) to the calculated cross-sections based on uniform charge distributions and the squares (□) correspond to calculated cross-sections with the positive charge largely located on the silver atoms (see [103]).

on the DFT calculations: for all compositions – except for the $Ag_3Au_2^+$ – the same structures as in the pure Au_5^+ and Ag_5^+ clusters are favored (i.e., two triangles, connected by a common central atom, "X-structure"). Within this topology, the silver atoms tend to have a maximum distance—a consequence of the positive partial charge localized on these atoms. In the case of $Ag_3Au_2^+$, however, the trigonal bipyramid is the global minimum, the X-structure is slightly, 0.03 eV, higher in energy. The cross-sections of these two structures are in good agreement with the values for the two isomers found in experiment (see Fig. 14).

4. Conclusion

To summarize, the combination of gas phase ion mobility spectrometry and quantum chemical calculations has proven to be extremely useful for the structure determination of cluster ions. Crucial for the success of this method is the fact that modern quantum chemical calculations are usually able to reproduce experimental geometry parameters to a high degree of accuracy, especially when looking for trends within a row of similar clusters. The calculations are however much less reliable with respect to the relative energies of different isomers. In this situation, the comparison of collision cross-sections allows us to distinguish between several energetically plausible structures.

For the small coinage metal cluster cations, we find a distinct difference between silver and copper on one hand and gold on the other hand. Positively charged silver and copper clusters tend to favor compact, three-dimensional structures for cluster sizes above five atoms, the respective gold clusters are planar up to the heptamer. In the mixed clusters, gold tends to be more electronegative, giving rise to highly polar bonds. In anionic gold clusters we observe a strong preference for planar structures. The unusual behavior of gold can be rationalized in terms of the lowering of the 6s orbitals relative to the 5d-shell due to relativistic effects, leading to an efficient s–d-hybridization allowing for more directed bonds.

Acknowledgements

I would like to thank Manfred M. Kappes for giving me the opportunity to build the ion mobility machine, for his ongoing support and for many inspiring discussions. I also thank Thomas Bierweiler, Elena Vollmer and Stefan Gilb for spending a lot of time in the laboratory taking data and for running countless calculations in search for the global minimum.

References

[1] J.S. Townsend, The diffusion of ions into gases, Phil. Trans. R. Soc. A 193 (1899) 129.
[2] A.M. Tyndall, The Mobilities of Positive Ions in Gases, Cambridge University Press, Cambridge, 1938.
[3] E.A. Mason, E.W. McDaniel, Transport Properties of Ions in Gases, Wiley, New York, 1988.
[4] For a review, see: G.A. Eiceman, Crit. Rev. Anal. Chem. 22 (1991) 471.
[5] G.A. Eiceman, Z. Karpas, Ion Mobility Spectrometry, CRC Press, Boca Raton, FL, USA, 1994.
[6] L.L. Danylewych-May, C. Cumming, in: J. Yinon (Ed.), Advances in Analysis and Detection of Explosives, Kluwer Academic, Dordrecht, 1993, p. 385.
[7] R.G. Ewing, D.A. Atkinson, G.A. Eiceman, G.J. Ewing, Talanta 54 (2001) 515.
[8] T. Khayamian, M. Tabrizchi, M.T. Jafari, Talanta 59 (2003) 327.
[9] G.A. Eiceman, J.A. Stone, Anal. Chem. 76 (2004) 390A.
[10] M.T. Bowers, P.R. Kemper, G.v. Helden, P.A.M. van Koppen, Science 260 (1993) 1446.
[11] G.v. Helden, M.T. Hsu, P.R. Kemper, M.T. Bowers, J. Chem. Phys. 95 (1991) 3835.
[12] M.F. Jarrold, V.A. Constant, Phys. Rev. Lett. 67 (1991) 2994.
[13] R.R. Hudgins, M.A. Ratner, M.F. Jarrold, J. Am. Chem. Soc. 120 (1998) 12974.
[14] R.R. Hudgins, M.F. Jarrold, J. Am. Chem. Soc. 121 (1999) 3494.
[15] R.R. Hudgins, M.F. Jarrold, J. Phys. Chem. B 104 (2000) 2154.
[16] D.T. Kaleta, M.F. Jarrold, J. Phys. Chem. B 105 (2001) 4436.
[17] B.S. Kinnear, M.R. Hartings, M.F. Jarrold, J. Am. Chem. Soc. 123 (2001) 5660.
[18] B.S. Kinnear, M.F. Jarrold, J. Am. Chem. Soc. 123 (2001) 7907.
[19] B.S. Kinnear, M.R. Hartings, M.F. Jarrold, J. Am. Chem. Soc. 124 (2002) 4422.
[20] M. Kohtani, T.C. Jones, J.E. Schneider, M.F. Jarrold, J. Am. Chem. Soc. 126 (2004) 7420.
[21] M. Kohtani, M.F. Jarrold, J. Am. Chem. Soc. 126 (2004) 8454.
[22] A.C. Gill, K.R. Jennings, Th. Wyttenbach, M.T. Bowers, Int. J. Mass Spectrom. 195/196 (2000) 685.
[23] T. Wyttenbach, M. Witt, M.T. Bowers, J. Am. Chem. Soc. 122 (2000) 3458.
[24] T. Wyttenbach, J.R. Batka, J. Gidden, M.T. Bowers, Int. J. Mass Spectrom. 193 (1999) 143.
[25] J. Gidden, E.S. Baker, A. Ferzoco, M.T. Bowers, Int. J. Mass Spectrom. 240 (2005) 183.
[26] J. Gidden, A. Ferzoco, E.S. Baker, M.T. Bowers, J. Am. Chem. Soc. 126 (2004) 15132.
[27] T. Wyttenbach, E.S. Baker, S.L. Bernstein, A. Ferzoco, J. Gidden, D. Liu, M.T. Bowers, Adv. Mass Spectrom. 16 (2004) 189.
[28] E.S. Baker, J. Gidden, A. Ferzoco, M.T. Bowers, Phys. Chem. Chem. Phys. 6 (2004) 2786.
[29] J. Gidden, M.T. Bowers, J. Am. Soc. Mass Spectrom. 14 (2003) 161.
[30] J. Gidden, M.T. Bowers, Eur. Phys. J. D 20 (2002) 409.
[31] J. Gidden, J.E. Bushnell, M.T. Bowers, J. Am. Chem. Soc. 123 (2001) 5610.
[32] J. Gidden, T. Wyttenbach, A.T. Jackson, J.H. Scrivens, M.T. Bowers, J. Am. Chem. Soc. 122 (2000) 4692.
[33] J. Gidden, T. Wyttenbach, J.J. Batka, P. Weis, M.T. Bowers, A.T. Jackson, J.H. Scrivens, J. Am. Soc. Mass Spectrom. 10 (1999) 883.
[34] J. Gidden, A.T. Jackson, J.H. Scrivens, M.T. Bowers, Int. J. Mass Spectrom. 188 (1999) 121.
[35] E.S. Baker, J. Gidden, S.E. Anderson, T.S. Haddad, M.T. Bowers, Nano Lett. 4 (2004) 779.
[36] C.A. Srebalus Barnes, A.E. Hilderbrand, S.J. Valentine, D.E. Clemmer, Anal. Chem. 74 (2002) 26.
[37] S. Myung, Y.J. Lee, M.H. Moon, J. Taraszka, R. Sowell, S. Koeniger, A.E. Hilderbrand, S.J. Valentine, L. Cherbas, P. Cherbas, T.C. Kaufmann, D.F. Miller, Y. Mechref, M.V. Novotny, M.A. Ewing, C.R. Sporleder, D.E. Clemmer, Anal. Chem. 75 (2003) 5137.

[38] C.S. Hoaglund-Hyzer, Y.J. Lee, A.E. Counterman, D.E. Clemmer, Anal. Chem. 74 (2002) 992.
[39] S.L. Koeniger, S.J. Valentine, S. Myung, M. Plasencia, Y.J. Lee, D.E. Clemmer, J. Proteome Res. 4 (2005) 25.
[40] R.A. Sowell, S.L. Koeniger, S.J. Valentine, M.H. Moon, D.E. Clemmer, J. Am. Soc. Mass Spectrom. 15 (2004) 1341.
[41] C.S. Creaser, J.R. Griffiths, C.J. Bramwell, S. Noreen, C.A. Hill, C.L.P. Thomas, Analyst 129 (2004) 984.
[42] T. Wyttenbach, M.T. Bowers, Top. Curr. Chem. 225 (2003) 207.
[43] M.F. Jarrold, Ann. Rev. Phys. Chem. 51 (2000) 179.
[44] A. Shvartsburg, M.F. Jarrold, Chem. Phys. Lett. 261 (1996) 86.
[45] G.v. Helden, N.G. Gotts, M.T. Bowers, Nature 363 (1993) 60.
[46] G.v. Helden, N.G. Gotts, M.T. Bowers, J. Am. Chem. Soc. 115 (1993) 4363.
[47] J. Hunter, J. Fye, M.F. Jarrold, Science 260 (1993) 784.
[48] J. Hunter, J.L. Fye, M.F. Jarrold, J. Chem. Phys. 99 (1993) 1785.
[49] K.B. Shelimov, J.M. Hunter, M.F. Jarrold, Int. J. Mass Spectrom. Ion Process. 138 (1994) 17.
[50] G.v. Helden, P.R. Kemper, N.G. Gottes, M.T. Bowers, Science 259 (1993) 1300.
[51] S. Lee, N. Goots, G.v. Helden, M.T. Bowers, J. Phys. Chem. A 101 (1997) 2096.
[52] J.M. Hunter, M.F. Jarrold, J. Am. Chem. Soc. 117 (1995) 10317.
[53] A.A. Shvartsburg, R.R. Hudgins, Ph. Dugourd, M.F. Jarrold, J. Phys. Chem. A 101 (1997) 1684.
[54] A.A. Shvartsburg, L.A. Pederson, R.R. Hudgins, G.C. Schatz, M.F. Jarrold, J. Phys. Chem. A 102 (1998) 7919.
[55] A.A. Shvartsburg, R.R. Hudgins, R. Gutierrez, G. Jungnickel, T. Frauenheim, K.A. Jackson, M.F. Jarrold, J. Phys. Chem. A 103 (1999) 5275.
[56] G.v. Helden, N.G. Gotts, P. Maitre, M.T. Bowers, Chem. Phys. Lett. 227 (1994) 601.
[57] J.L. Fye, M.F. Jarrold, J. Phys. Chem. A 101 (1997) 1836.
[58] K. Shelimov, M.F. Jarrold, J. Phys. Chem. 99 (1995) 17677.
[59] K. Shelimov, D.E. Clemmer, M.F. Jarrold, J. Phys. Chem. 98 (1994) 12819.
[60] K. Shelimov, M.F. Jarrold, J. Am. Chem. Soc. 117 (1995) 6404.
[61] K. Shelimov, M.F. Jarrold, J. Am. Chem. Soc. 118 (1996) 1139.
[62] D.E. Clemmer, M.F. Jarrold, J. Am. Chem. Soc. 117 (1995) 8841.
[63] M.F. Jarrold, J.E. Bower, J. Chem. Phys. 98 (1993) 2399.
[64] M.F. Jarrold, J.E. Bower, J. Chem. Phys. 97 (1993) 1746.
[65] J. Lermé, P. Dugourd, R.R. Hudgins, M.F. Jarrold, Chem. Phys. Lett. 304 (1999) 19.
[66] B. Baguenard, M. Pellarin, C. Bordas, J. Lermé, J.L. Vialle, M. Broyer, Chem. Phys. Lett. 205 (1993) 13.
[67] G.v. Helden, P.R. Kemper, M.T. Hsu, M.T. Bowers, J. Chem. Phys. 96 (1992) 6591.
[68] M.F. Jarrold, J.E. Bower, J. Chem. Phys. 96 (1992) 9180.
[69] K.-M. Ho, A.A. Shvartsburg, B. Pan, Z.-Y. Lu, C.-Z. Wang, J.G. Wacker, J.L. Fye, M.F. Jarrold, Nature 392 (1998) 582.
[70] R.R. Hudgins, M. Imai, M.F. Jarrold, P. Dugourd, J. Chem. Phys. 111 (1999) 7865.
[71] A.A. Shvartsburg, B. Liu, Z.-Y. Lu, C.-Z. Wang, M.F. Jarrold, K.-M. Ho, Phys. Rev. Lett. 83 (1999) 2167.
[72] M.F. Jarrold, J. Phys. Chem. 99 (1995) 11.
[73] A.A. Shvartsburg, M.F. Jarrold, Phys. Rev. A 60 (1999) 1235.
[74] A.A. Shvartsburg, M.F. Jarrold, Phys. Rev. Lett. 85 (2000) 2530.
[75] A.A. Shvartsburg, M.F. Jarrold, Chem. Phys. Lett. 317 (2000) 615.
[76] C.W. Bauschlicher, S.R. Langhoff, H. Partridge, J. Chem. Phys. 91 (1989) 2412.
[77] D. Liao, K. Balasubramanian, J. Chem. Phys. 97 (1992) 2548.
[78] V. Bonačić-Koutecký, L. Češpiva, P. Fantucci, J. Koutecký, J. Chem. Phys. 98 (1993) 7981.
[79] V. Bonačić-Koutecký, J. Pittner, M. Boiron, P. Fantucci, J. Chem. Phys. 110 (1999) 3876.
[80] J. Yoon, K.S. Kim, K.K. Baeck, J. Chem. Phys. 112 (2000) 9335.
[81] R. Mitrić, M. Hartmann, B. Stanca, V. Bonačić-Koutecký, P. Fantucci, J. Phys. Chem. A 105 (2001) 8892.
[82] D. Schooss, S. Gilb, J. Kaller, M.M. Kappes, F. Furche, A. Kohn, K. May, R. Ahlrichs, J. Chem. Phys. 113 (2000) 5361.
[83] M. Vogel, A. Herlet, L. Schweikhart, J. Am. Soc. Mass Spectrom. 14 (2003) 614.
[84] S. Yang, V.A. Spasov, K.M. Ervin, J. Chem. Phys. 111 (1999) 938.
[85] S. Wolf, G. Sommerer, S. Rutz, E. Schreiber, T. Leisner, L. Wöste, R.S. Berry, Phys. Rev. Lett. 74 (1995) 4177.
[86] H. Hess, K.R. Asmis, T. Leisner, L. Wöste, Eur. Phys. J. D 16 (2001) 145.
[87] C. Félix, C. Sieber, W. Harbich, J. Buttet, I. Rabin, W. Schulze, G. Ertl, Phys. Rev. Lett. 86 (20012992).
[88] P. Weis, S. Gilb, P. Gerhardt, M.M. Kappes, Int. J. Mass Spectrom. 216 (2002) 59.
[89] (a) T.G. Dietz, M.A. Duncan, D.E. Powers, R.E. Smalley, J. Chem. Phys. 74 (1981) 6511;
(b) P. Milani, W.A. deHeer, Rev. Sci. Instrum. 61 (1990) 1835.
[90] P. Weis, T. Bierweiler, S. Gilb, M.M. Kappes, Chem. Phys. Lett. 355 (2002) 355.
[91] B. Becke, Phys. Rev. A 38 (1988) 3098;
J. Perdew, Phys. Rev. B 33 (1986) 8822.
[92] R. Ahlrichs, M. Baer, H. Horn, C. Koelmel, Chem. Phys. Lett. 162 (1989) 165 (see http://www.turbomole.de for the current version).
[93] D. Andrae, U. Haeussermann, M. Dolg, H. Stoll, H. Preuss, Theor. Chim. Acta 77 (1990) 123.
[94] V. Bonačić-Koutecký, L. Češpiva, P. Fantucci, J. Koutecký, J. Chem. Phys. 98 (1993) 7981.
[95] K. Jug, B. Zimmermann, P. Calaminici, A.M. Köster, J. Chem. Phys. 116 (2002) 4497.
[96] S. Gilb, P. Weis, F. Furche, R. Ahlrichs, M.M. Kappes, J. Chem. Phys. 116 (2002) 4094.
[97] P. Pyykkö, Angew. Chem. 116 (2004) 4512;
H. Schwarz, Angew. Chem. Int. Ed. 42 (2003) 4442.
[98] P. Weis, T. Bierweiler, E. Vollmer, M.M. Kappes, J. Chem. Phys. 117 (2002) 9293.
[99] F. Furche, R. Ahlrichs, P. Weis, C. Jacob, S. Gilb, T. Bierweiler, M.M. Kappes, J. Chem. Phys. 117 (2002) 6982.
[100] J.C. Fabbi, J.D. Langenberg, Q.D. Costello, M.D. Morse, L. Karlsson, J. Chem. Phys. 115 (2001) 7543.
[101] Y. Negishi, Y. Nakamura, A. Nakajima, K. Kaya, J. Chem. Phys. 115 (2001) 3657.
[102] V. Bonačić-Koutecký, J. Burda, R. Mitrić, M. Ge, G. Zampella, P. Fantucci, J. Chem. Phys. 117 (2002) 3120.
[103] P. Weis, O. Welz, E. Vollmer, M.M. Kappes, J. Chem. Phys. 120 (2004) 677.